Lab on a Chip

PAPER

View Article Online
View Journal

Cite this: DOI: 10.1039/d5lc01055a

A microfluidic method for controlled generation and trapping of membraneless water-in-water droplets

Chi Li, †[ab] Hailin Fu, †*[cd] Kalpit J. Bakal, [ab] Jaap M. J. den Toonder, [abd] E. W. Meijer, [cd] Sailing He*[a] and Hans M. Wyss *[abd]

Received 15th November 2025,
Accepted 7th March 2026

DOI: 10.1039/d5lc01055a

rsc.li/loc

Aqueous two-phase systems (ATPS) provide a versatile platform for controlling microscale aqueous environments. Microfluidic devices are particularly valuable for studying such systems, as they allow precise control of geometry, flow, and composition. However, understanding the dynamic behavior of ATPS requires studying the time-dependent exchange between the two phases, which is difficult in existing, water-in-oil microfluidic setups, where the overall composition within each ATPS droplet remains fixed. Here we introduce an oil-free platform that creates ATPS droplets *in situ via* liquid–liquid phase separation in dead-end chambers, with time-dependent control of the chemical composition in the channel and tunable exchange kinetics set by the connecting geometry. The approach is remarkably robust, reliably forming stable droplets without surfactants or fine flow control. We validate the platform by demonstrating precise droplet control for the well-studied PEG–dextran ATPS, and use it to study an associative coacervate (PAA/PDMAEMA) system, where we observe reversible sub-compartment formation, highlighting the platform's potential for dynamic studies of multiphase systems.

Introduction

Droplet microfluidics, which manipulates tiny fluid volumes in channel-based systems, has revolutionized research in areas such as single-cell RNA sequencing, single-molecule proteomics, high-throughput drug screening, protein crystallization, or the mapping of phase diagrams.[1–3] Traditionally, most droplet-based platforms use water-in-oil (W/O) emulsions, in which aqueous droplets are suspended in a continuous oil phase.[4–6] These systems benefit from high interfacial tension, enabling rapid and uniform droplet formation. However, the immiscibility between water and oil presents a major limitation: solute exchange between droplets and their environment is severely restricted.[7] This makes real-time modulation of droplet composition, long-term incubation, and the study of dynamic, out-of-equilibrium processes challenging.

Aqueous two-phase systems (ATPS) offer an alternative by enabling the formation of water-in-water (W/W) droplets in an oil- and surfactant-free environment.[8] These systems allow unhindered diffusion of water-soluble molecules (*e.g.*, nutrients, metabolites, synthetic probes), supporting open-system behavior, long-term viability of encapsulated cells, and new possibilities for synthetic cell biology.[9,10] Yet, the extremely low interfacial tensions between two aqueous phases (0.001–0.1 mN m^{-1}) make droplet stabilization difficult,[11,12] often requiring additional surfactants or structural confinement.[13,14] Furthermore, current methods for spatially controlling W/W droplets with such low interfacial tension typically rely on precise flow modulation or external fields (*e.g.*, acoustic or optical forces), whose biochemical effects remain largely uncharacterized.[6,15–17]

Despite the promise of W/W droplet systems, what is still missing is a simple, scalable way to precisely localize and retain droplets while continuously and reversibly exchanging their surrounding chemical environment. Without this capability, it remains difficult to study how LLPS systems dynamically respond to matter exchange and environmental cues, or to investigate structure formation under out-of-equilibrium conditions—features that are central to many biological and synthetic processes. In this paper, we present an oil-free microfluidic platform that enables *in situ*

[a] *IDEAS ZJU-TU/e Joint Research Institute of Design, Optoelectronics and Sensing, College of Optical Science and Engineering, Zhejiang University, 866 Yuhangtang Road, Hangzhou, 310058, Zhejiang, China. E-mail: sailing@zju.edu.cn*
[b] *Department of Mechanical Engineering, Eindhoven University of Technology, De Zaale 5, Eindhoven, 5612 AE, Noord Brabant, The Netherlands. E-mail: H.M.Wyss@tue.nl*
[c] *Department of Chemistry and Chemical Engineering and Laboratory of Macromolecular and Organic Chemistry, Eindhoven University of Technology, De Zaale 5, Eindhoven, 5612 AE, Noord Brabant, The Netherlands. E-mail: h.fu@tue.nl*
[d] *Institute for Complex Molecular Systems (ICMS), Eindhoven University of Technology, De Zaale 5, Eindhoven, 5612 AE, Noord Brabant, The Netherlands*
† These authors contributed equally to this work.

generation and stable trapping of size-controlled W/W droplets inside dead-end chambers, without the need of surfactants, oil phases, or surface-tension-based droplet traps. Unlike conventional systems, where droplets are formed through interfacial shear at immiscible phase boundaries, droplet formation in our system is driven by controlled diffusion and phoretic transport of polymer solutions and intrinsic ATPS phase separation. The key parameters governing droplet formation are the neck geometry and the exposure time to flows applied in the main channel, rather than flow rate or mechanical perturbation. This makes droplet formation in these devices remarkably robust and enables us to study the response of LLPS systems to dynamically changing conditions.

Critically, our system is not just another example of a microfluidic system that studies LLPS within microfluidic water-in-oil droplets. Such systems can be very powerful for instance for high-throughput mapping of phase diagrams; however, they have limitations in modulating the chemical environment (polymer concentrations, salt concentrations, pH) and observing the dynamic response to changes in chemical environment that occur in the system. It is a truly open system: each chamber is connected to a main channel carrying aqueous solution of controlled composition, enabling dynamic matter exchange and reversible modulation of chemical conditions around the aqueous droplets.

Validation using the PEG–dextran model system—a well-characterized segregative ATPS (where solutes repel each other)—demonstrates the platform's capability of precise W/W droplet formation, achieving controlled droplet size and concentration. To illustrate the versatility of our approach, we also applied it to associative LLPS (where solutes associate with each other), using a poly(acrylic acid) (PAA)/poly(*N*,*N*-dimethylaminoethyl methacrylate) (PDMAEMA) coacervate system as an example, to achieve tunable coacervate droplet formation. Notably, in this system we also observed the kinetic formation of internal compartments within coacervate droplets in response to the flow state in the main channel. In addition, by integrating pneumatically activated valves between adjacent chambers in our devices, we can enable molecular exchange between chambers, thus further reinforcing the open nature and controllability of our system.

Altogether, the platform offers powerful means for probing the dynamic behavior of LLPS systems under static as well as chemically evolving conditions. While it may not be optimized for rapid phase diagram mapping, it enables in-depth mechanistic studies of transitions between LLPS states and structure formation in water-in-water systems and demonstrates great potential for *in situ* modulation of chemical reactions, long-term incubation of cells and dynamic control of drug exposure time and load in drug screening—advancing both fundamental research and applications in soft matter, synthetic biology, biochemical engineering and pharmaceutics.

Results

Schematic Fig. 1 illustrates a conceptual comparison between conventional droplet microfluidics and our proposed oil-free W/W droplet platform. In traditional water-in-oil (W/O) systems, droplets are typically formed at a T-junction or flow-focusing through interfacial shear forces, driven by the high interfacial tension between aqueous and oil phases. While this method ensures high droplet uniformity and throughput, it inherently restricts solute exchange and necessitates surfactants or oil matrices that may interfere with biological or chemical processes. Moreover, W/O droplets act as a closed system, limiting their utility in scenarios requiring continuous biochemical modulation.

In contrast, water-in-water (W/W) droplet systems, based on aqueous two-phase separation, possess significantly lower interfacial tension, enabling open molecular exchange but suffering from poor stability and weak confinement. Our platform circumvents these limitations by decoupling droplet formation from interfacial shear and surfactant dependence. Instead, droplets are generated *in situ via* diffusion-mediated phase separation in geometrically confined dead-end chambers, allowing for spontaneous formation, stable retention, and reversible molecular transport. Below we describe in detail our microfluidic platform and the method for generating aqueous two-phase W/W droplets.

Design of microfluidic chips

The microfluidic chip used in this work has three main components: a main channel with an inlet and an outlet, a series of dead-end chambers or traps, and junction necks connecting the main channel and dead-end chambers (Fig. 2a). The chambers are designed to be cylindrical with a height of $h_{\mathrm{chamb.}}$, which is equal to the height of the main channel. The chamber dimensions are kept the same throughout the microfluidic device. However, to control the trafficking of molecules between the main channel and the chambers, the geometry of the junction necks is tuned with varying widths w_{n} and lengths l_{n}. The height of the necks is generally fixed at $h_{\mathrm{n}} = h_{\mathrm{chamb.}}/2$. To create these microfluidic structures, we employed the femtosecond laser micromachining (FLM) method to generate patterns in fused silica. In this fabrication method, 3D scanning exposure with focused femtosecond laser pulses is used to modify the microscopic structure of a substrate material within defined regions.[18] Subsequently, a wet etching step with potassium hydroxide removes the exposed regions, thereby creating 3-dimensional structures in glass (Fig. S1a and b, SI).

Choosing the FLM method in glass over a more traditional soft lithography process (shown schematically in Fig. S7a–c) using polydimethylsiloxane (PDMS) has several important advantages. As glass is inherently impermeable to gases and liquids, changes in concentration due to evaporation can be circumvented, even when samples are kept in the channels over extended periods of time. Moreover, in PDMS devices, macromolecules can diffuse into the walls of the device over time, which can lead to significant changes in experimental

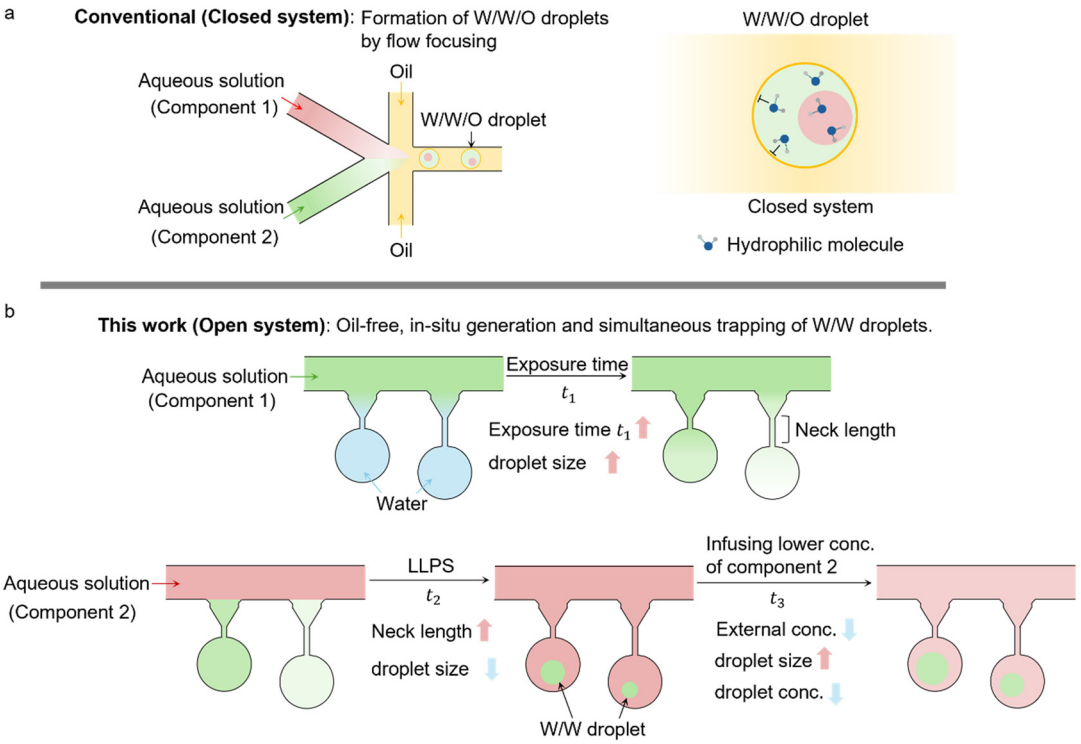

Fig. 1 Comparison between traditional closed water-in-water-in-oil (W/W/O) droplet microfluidics and open water-in-water (W/W) droplet systems in this work. a, Conventional W/W/O droplet formation relies on shear forces during flow-focusing with high interfacial tension ($\gamma_{W/O}$); W/W/O droplet as a closed system limit molecular exchange between the droplet and the surrounding oil phase. b, Schematic illustration of our oil-free platform: polymer concentration gradients induce transport of solutes into the dead-end chambers and W/W droplets are formed *in situ via* ATPS phase separation without external forces or surfactants. The system allows for tunable control of droplet size and concentration in a highly robust manner, insensitive to the flow rates applied in the main channel. Longer exposure time (t_1) to component 1 results in bigger droplets; longer neck length leads to smaller droplets; in addition, the droplet's concentration is controlled by equilibrium with component 2 in the main channel. For instance, infusing lower concentrations of component 2 after equilibrium (t_3) will lead to larger droplets with lower concentrations.

conditions. This is illustrated in Fig. S7d, where we show that macromolecules can readily diffuse into the PDMS material, while fused silica is practically impenetrable, thus ensuring long-term stability of the experimental conditions.[19]

Validation using the PEG–dextran system

To demonstrate the functionality of our microfluidic device, we validate it on the well-known polyethylene glycol (PEG)–dextran system, which undergoes segregative-type liquid–liquid phase separation (LLPS), to generate dextran droplets within the dead-end chambers. The PEG–dextran system is a well-established reference;[20] its phase diagram, illustrated schematically in Fig. 2b, delineates the one-phase, homogeneously mixed region from the two-phase region, with dextran concentration on the horizontal axis and the PEG concentration on the vertical axis. A solution within the two-phase region (indicated as 2θ) will undergo phase separation along the tie lines, resulting in a dextran-rich phase and a PEG-rich phase. Prior to droplet formation, the microfluidic chip is filled with deionized (DI) water, utilizing a vacuum-assisted protocol detailed in the SI. The PEG and dextran solutions are distinguished by the fluorescent labels PEG-rhodamine (red) and dextran-fluorescein isothiocyanate (FITC, green), respectively. As a typical example, the formation of dextran droplets is executed in two principal steps:

Step 1: a 10 wt% dextran solution is introduced into the main channel at a constant flow rate of 100 μL h^{-1} for a predetermined duration t_1. In the example depicted in Fig. 2, a duration of t_1 = 120 minutes is selected. Following the initiation of this flow of dextran solution, we observe a continuous increase in the fluorescence intensity in chambers, as shown in Fig. 2c. The concentration of dextran in the chamber reaches C_{Dex} (Fig. 2b) right before step 2.

Step 2: the flow of dextran solution in the main channel is replaced by a constant flow of PEG solution with a pre-determined concentration (C_{PEG} in Fig. 2b). As PEG diffuses into the dead-end channels, we observe phase separation and the formation of dextran-rich droplets within chambers. Upon reaching a quasi-equilibrium, the PEG concentration within the dead-end chamber matches that in the main channel (C_{PEG} in Fig. 2b), resulting in stable dextran droplets with a concentration (C_{in} in Fig. 2b) controlled by the applied PEG concentration, as dictated by the PEG–dextran phase diagram. Note that the diffusion of dextran into the main channel is significantly suppressed due to its low solubility in concentrated PEG solution.

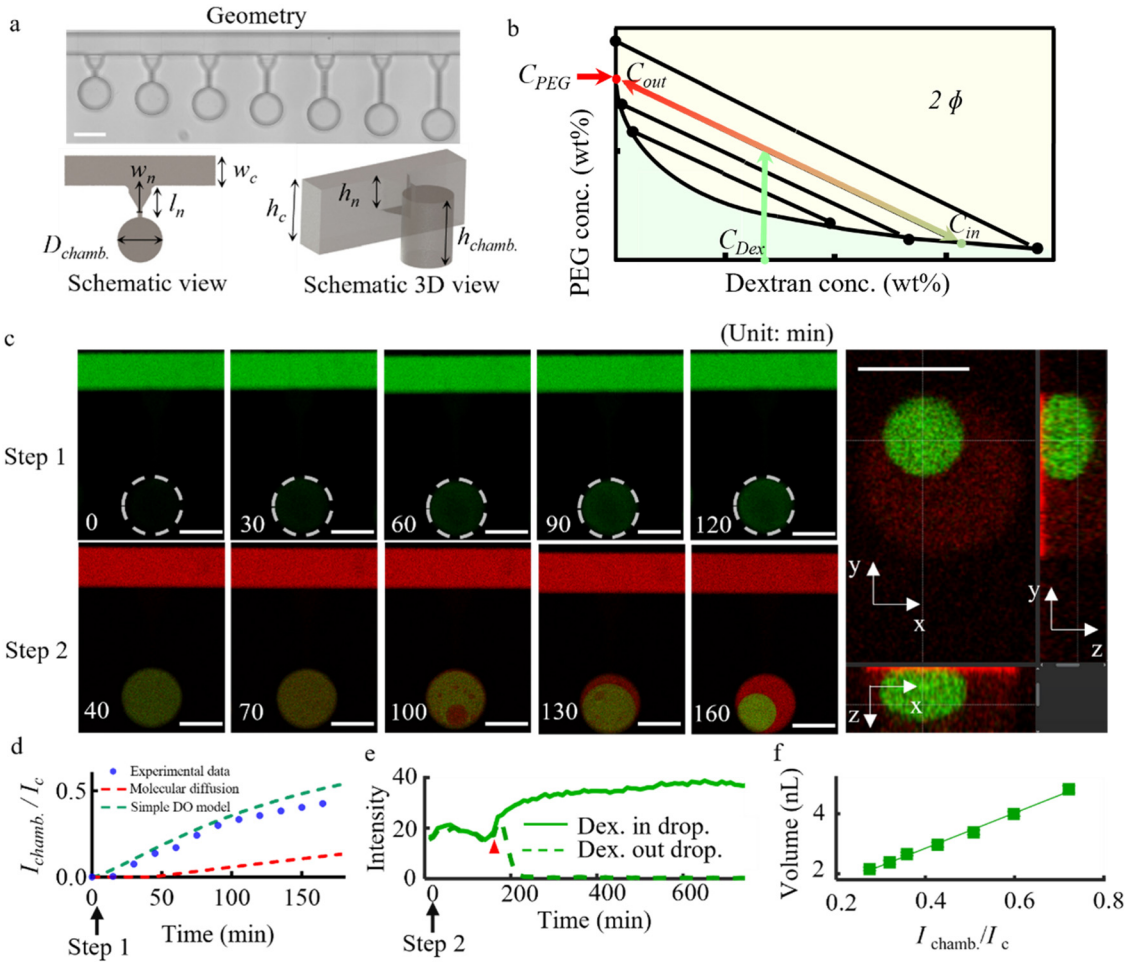

Fig. 2 Formation and trapping of dextran droplets formed *via* liquid–liquid phase separation (LLPS) in a microfluidic device with dead-end chambers. a, Microfluidic chip design featuring dead-end chambers, with channel width w_c = 200 μm, channel height h_c = 400 μm, chamber diameter $D_{chamb.}$ = 300 μm, and chamber height $h_{chamb.}$ = 400 μm. The neck dimensions (w_n and l_n) are adjusted, ranging from 30 μm to 90 μm for width and 60 μm to 360 μm for length, respectively. Scale bar: 300 μm. b, Representative phase diagram for the PEG–dextran aqueous two-phase system. c, Stepwise process of LLPS in dead-end chambers; **step 1**: visualized diffusion of the dextran solution (green, labelled with dextran-FITC) into the dead-end chamber over time, with a continuous flow through the main channel maintaining a constant dextran concentration in the channel; **step 2**: initiation of phase separation following the injection of PEG solution (red, labelled with PEG-rhodamine) and its diffusion into the dead-end chambers. **Panel at the right**: three-dimensional shape of a formed dextran droplet, as visualized by three confocal microscopy sections in the *xy*-, *xz*-, and *yz*-planes, respectively. The depicted chamber features a neck width of w_n = 30 μm. Scale bars are 200 μm. d, Experimental data (blue dots) and numerical models (red dashed line: diffusion model; green dashed line: diffusio-osmosis model; see SI for details) for the relative dextran concentration within the chamber (l_n = 210 μm, w_n = 30 μm) as a function of dextran exposure time by infusing 10 wt% dextran solution into the microfluidic chip. I_c.: intensity in the main channel, $I_{chamb.}$: intensity in the chamber. e, Temporal changes in dextran concentrations inside and outside the forming droplets, with the arrow indicating the onset of LLPS. f, Correlation between the droplet volume and the relative fluorescence intensity of dextran within the traps.

During step 1, we monitored the fluorescence intensity dynamics of dextran-FITC within the chamber and observed that the concentration of dextran in the chamber increased at a rate faster than initially anticipated. The red dashed line in Fig. 2d presents the predicted evolution of dextran concentration in the chamber based only on the molecular diffusion of dextran 500 kDa. Notably, this theoretical projection lagged significantly behind the actual experimental data (blue dots in Fig. 2d). These discrepancies led us to hypothesize that besides molecular diffusion, diffusio-osmosis – the convective transport of liquid along a surface, driven by a concentration gradient – also plays a critical role in the process of dextran molecules entering the chamber. To test this hypothesis, we develop a simple, analytical diffusio-osmosis model for the transport of dextran solution through the connecting channel that also incorporates a contribution from molecular diffusion inside the chamber. The result, depicted by the green dashed line in Fig. 2d, shows a reasonable agreement with the experimental data. This illustrates that the contribution of diffusio-osmosis is significant and that molecular diffusion alone cannot account for the transport of dextran into our chambers. Nevertheless, the interplay between diffusio-osmotic convection and molecular diffusion in this complex

geometry cannot be fully captured by a simple analytical model; this would require a detailed 3D numerical simulation, which goes beyond the scope of the current study. The detailed analytical derivations for both the diffusion model and the analytical diffusio-osmosis model are provided in SI.

To track the phase separation process in real-time, fluorescence intensities of dextran-FITC and PEG-rhodamine are monitored simultaneously in step 2 using confocal microscopy. Initially, the fluorescence intensity of PEG-rhodamine increases and the dextran-FITC signal in the chambers remains nearly constant. Subsequently, droplets suddenly appear, marking the commencement of phase separation (Fig. 2c). Capturing the three-dimensional shape of a droplet by sections through the *xy*-, *xz*-, and *yz*-planes in the confocal microscope, we observe a visibly non-spherical droplet shape as a result of the differences in density between the two phases and the low surface tension. The formation of dextran droplets is accompanied by a sudden increase of the green fluorescence intensity in the droplet area and a dramatic drop of the green signal outside of the droplet area, ascertaining the spinodal phase separation process, as shown in Fig. 2e. The saturation of the green fluorescence intensity inside droplets (I_{Dex}) indicates the establishment of a quasi-equilibrium. While the PEG concentration (C_{PEG}) in the main channel can regulate the concentration of dextran droplets (C_{in}) dictated by the phase diagram (Fig. 2b), the volume of droplets ($V_{droplet}$) should be tunable by controlling the total amount of dextran ($V_{chamber} \times C_{Dex}$) diffused into chambers in step 1 (eqn (1)). To verify this idea, we systematically analyze the equilibrium droplet volumes for chambers with different green fluorescence intensities at the end of step 1 by integrating *z*-stacked imaging layers of droplets using a Matlab script. Indeed, as shown in Fig. 2f, we find a linear relationship between droplet volume ($V_{droplet}$) and final dextran-FITC fluorescence intensity ($I_{Dex} \propto C_{Dex}$) in step 1, confirming that droplet size can be directly controlled *via* the amount of dextran diffusing into each chamber ($V_{chamber} \times C_{Dex}$) in step 1.

$$V_{droplet} = \frac{V_{chamber}}{C_{in}} c_{Dex} \quad (1)$$

Our results corroborate the efficacy of this method in consistently producing water-in-water (W/W) droplets with finely tuned attributes in different experimental setups; specifically, concentration and volume of dextran droplets in PEG solution can be independently tuned by choosing initial PEG concentration and flow time of dextran solution, as well as by changing the design of the geometrical features in the chip, as we show below. Movies S1–S4 elucidate the progression of dextran diffusion into the dead-end chambers and the ensuing droplet formation process in both fluorescent and bright-field imaging modes.

Control over droplet size and concentration

To verify the influence of PEG concentration in the main channel on the dextran concentration in formed droplets, after step 1, we sequentially apply a flow of PEG solutions of decreasing concentrations (12, 10, 9, 8, 7, and 6 wt%) in the main channel; for each solution, we maintain a constant flow rate of 100 μL h^{-1} for at least 6 hours before imaging. We find that with decreasing PEG concentrations, all droplets expand in size (Fig. 3a, top), while simultaneously the green fluorescence intensities decrease (Fig. 3a, bottom); see Movies S5–S8 for further examples of this behavior. Dextran concentrations inside the droplets and PEG concentrations in the main channel are extracted from calibrated fluorescence intensity curves. We find that the relationship between these concentrations generally agrees with the schematic phase diagram (Fig. 3b and S2a–d, SI). This confirms that the dextran concentration in droplets (C_{in}) can be readily controlled by varying the concentration of PEG flowing in the main channel (C_{PEG}) of our devices, as dictated by the phase diagram of the system.

Next, we explore the effect of diffusion on droplet size in depth by studying the impact of both the dextran exposure time applied in step 1 and the neck geometry. To demonstrate the effect of neck geometry, dead-end chambers comprising seven different neck lengths (from 60 μm to 360 μm with 50 μm intervals) and eight different neck widths (from 30 μm to 100 μm with 10 μm intervals) are integrated into a single device with each geometry repeated three times, giving rise to 56 different neck geometries and a total of 168 dead-end chambers (top of Fig. 3c). Repeating the two-step procedure described above, we obtain droplets of different sizes in all these chambers within one single experiment (bottom of Fig. 3c). Volume analysis from integrating over *z*-stacked fluorescent images shows that the droplet volume increases linearly with neck width and decreases linearly with neck length, suggesting that the diffusion or loading rate of dextran in step 1 is governed by both neck length and width (Fig. 3d, S4c and d SI).

To examine the effect of dextran exposure time in step 1 on the volume, three different dextran exposure times (1 hour, 2.75 hours and 4 hours) are used in step 1 followed by the same procedure in step 2. A volume analysis from three selected geometries (9 chambers in total) shows that the droplet volume increases with dextran exposure time in step 1 but this effect saturates at long exposure times, as shown in Fig. 3e and S4b. In addition, to predict the final droplet size by controlling the exposure time in step 1 (t_1), we established a diffusion model to simulate the dextran concentration variation in the dead-end chamber. However, the result shows that the predicted value of the dextran concentration in the dead-end chamber is much lower than the experimental value after a certain period. Considering the particle size of dextran-500 kDa and the osmotic pressure under different dextran concentrations, we find that the diffusion phoresis effect is the main reason mediating the change of dextran concentration in the dead-end

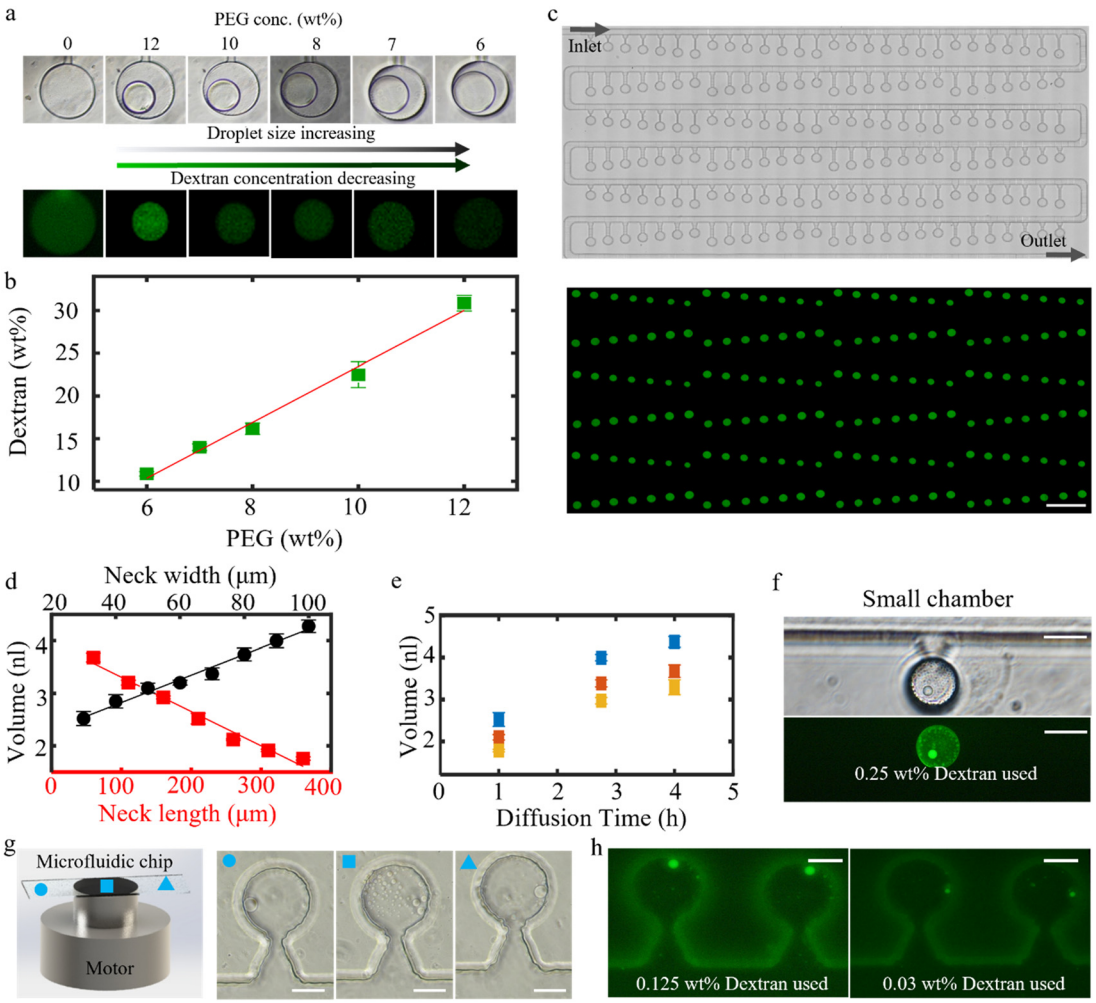

Fig. 3 Precise manipulation of the dextran concentration and size of the droplets within a silica-based microfluidic chip. a, Variability in the dextran concentration and size of the droplets achieved by injecting PEG solutions of incrementally decreasing concentrations into the main channel. Scale bar 100 μm. b, The relationship between the external PEG concentration and the internal dextran concentration. c, Top: bright field image showing the overall structure of the silica-based microfluidic chip before the generation of dextran droplets. Bottom: tile-scanning confocal fluorescence image of the same device, taken after the formation of dextran droplets in the chambers; the differences in droplet sizes illustrate the effects of neck geometry and diffusion duration. Scale bar is 1 mm. d, Control of dextran droplet volume by altering the geometry of the neck connecting the channel and chamber; the volume of the droplets decreases with increasing neck length (fixed neck width w_n = 50 μm, red squares and bottom axis) and increases with increasing neck width (fixed neck length l_n = 210 μm, black circles and top axis); linear fits to the data (solid lines) indicate an approximately linear behavior in both cases. 10 wt% dextran and 10 wt% PEG used here in step 1 and step 2, respectively. e, Control of dextran droplet volume as a function of the diffusion duration of 10 wt% dextran applied in step 1 and 10 wt% PEG in step 2; different colors represent different neck geometries (h_n = 200 μm and w_n = 50 μm for all, neck length of 160 μm, 260 μm, 310 μm, for blue, red, and yellow symbols, respectively). f, Formation of miniature dextran droplets using a downsized (50 μm diameter) dead-end chamber. g, Generation of miniature dextran droplets at low dextran concentrations, assisted by centrifugal force applied according to the schematic illustration shown on the left. The blue circle, square, and triangle correspond to the microfluidic chip's left, middle, and right regions, respectively. h, Formation of miniature dextran droplets assisted by centrifugal force, visualized by fluorescence microscopy. Scale bars in f–h represent 50 μm.

chamber, and the theoretically predicted value based on this effect is consistent with the experimental results.

To study the uniformity of droplet formation in our system, we perform a size analysis in a separate device comprising five kinds of geometries with 56 replicates for each geometry. As shown in Fig. S3, we obtain a low coefficient of variation CV ~2% for the droplet size. This is significantly better than for conventional microfluidic methods, where typically a CV of no lower than ~10% has been achieved for water-in-water (W/W) droplets.[21]

Finally, we aim to exercise our knowledge learned above by addressing the challenge of obtaining uniform droplets of small sizes (diameters <10 μm), which is difficult if not impossible using conventional microfluidic methods. To achieve this target, we aim to reduce the total amount of dextran introduced into a chamber, which should be translated directly into a smaller size of formed droplets. One way to achieve a lower total amount of dextran entering chambers is to simply reduce the size of dead-end chambers. Indeed, as shown in the example in Fig. 3f, in miniature chambers (with a much smaller diameter

of 50 μm), we obtain a miniature dextran droplet of only ~10 μm in diameter by using 0.25 wt% of dextran. Another approach to achieve miniature dextran droplets is to reduce the dextran exposure time and the concentration of dextran in the main channel. To test this approach, we employ dextran solutions of lower concentrations (0.125 wt% and 0.03 wt%) combined with a shorter exposure time (1–2 min) in step 1 of the process. At these low dextran concentrations, instead of the formation of a single dextran-rich droplet, we observe the formation of a multitude of small droplets of broad size distribution throughout dead-end chambers, as shown in Fig. 3g (middle image, marked with a square symbol). To obtain a single miniature droplet, we make use of centrifugation by spinning the microfluidic chip at 600 rpm, as indicated by the schematic in Fig. 3g. As a result, in the chambers located at the periphery of the microfluidic chip, where the centrifugal force acts, we observe the formation of a single miniature dextran droplet formed *via* the coalescence of multiple smaller droplets (Fig. 3g, images marked by triangle and circle). Fluorescence imaging, shown in Fig. 3h, reveals the formation of single miniature droplets more clearly, where the droplet size depends on the dextran concentration applied in the main channel. For a dextran concentration of c_1 = 0.125 wt% we obtain a small droplet diameter of $d_1 \sim 8$ μm, while for a concentration of c_2 = 0.03 wt% we obtain a smaller droplet, with $d_2 \sim 5$ μm. This is consistent with the expected scaling behavior in which we assume that the total amount of dextran in each case is proportional to the applied concentration, as $c_1/c_2 = (d_1/d_2)$.[3] This scaling implies that the volume of the miniature dextran droplet can be readily controlled to be as small as we wish by reducing the applied dextran concentration. Such miniature droplets can have meaningful applications, for example in artificial cell research. Alternatively, to avoid the spinning process, much smaller chambers can be designed for miniature droplets.

Application to associative LLPS

After having validated our methodology with the well-established PEG–dextran system, to illustrate the versatility of our microfluidic method, we apply it to the study of associative liquid–liquid phase separation and the controlled formation of complex coacervates. Associative liquid–liquid phase separation (LLPS) systems are characterized by their ability to compartmentalize —a feature fundamental to biological organization. This capacity allows for the assembly of diverse proteins, RNA and DNA, which is crucial for key cellular processes such as protein synthesis and RNA transcription, and it holds promise for the discovery of disease biomarkers. Mimicking the complex functions of living cells or membraneless organelles necessitates the creation of protocells with hierarchical structures featuring multiple compartments for the organization of materials and biochemical reactions. The dynamics of LLPS droplets offer a multi-compartmentalization strategy for the precise spatiotemporal regulation of reaction networks.[22]

To test our method in the context of associative LLPS, we use a binary system consisting of poly(acrylic acid) (PAA) and poly(*N*,*N*-dimethylaminoethyl methacrylate) (PDMAEMA), a well-studied system for which the phase diagram has been determined experimentally by Spruijt *et al.*,[23] as shown schematically in Fig. 4a. The phase diagram displays the concentration of PAA in both the dilute phase (hollow circle on the *x*-axis) and the coacervate phase (solid circle on the *x*-axis) as a function of salt concentration, where the salt concentrations in the two phases are assumed to be equal.

To initiate the formation of coacervates in the microfluidic chambers, akin to the procedure employed for the segregative PEG–dextran system, the device is initially filled with deionized water. After this, in **Step 1**, we apply a flow of a solution of PAA (0.33 M) and PDMAEMA (0.33 M) at a salt concentration of 1.5 M KCl in the main channel of the device. As a result, the salt and polymer concentrations in the chambers increase over time. As the system is in the one-phase region of the phase diagram at the applied 1.5 M KCl concentration as shown in the phase diagram, we do not observe phase separation at this stage. Subsequently, in **Step 2**, we switch the fluid flow in the main channel to a 1.2 M KCl solution, at which condition, according to the schematic phase diagram in Fig. 4a, we expect phase separation to occur. Additionally, to optimize the coalescence of separated droplets, the microfluidic chip is tilted to a vertical position, allowing any discrete droplets to merge on the concave side of the dead-end chamber driven by gravity.

Indeed, we observe phase separation within chambers as a result of this change in experimental conditions; as shown in Fig. 4b, discrete coacervates are formed throughout the fluidic chambers within the first 5 minutes after initiating the flow of the 1.2 M KCl solution in the main channel. Under the influence of gravity, within around 30 minutes, small coacervates gather on the bottom concave surface of the dead-end chamber. After 60 minutes, we observe that a single coacervate comprising multiple internal compartments has formed through the coalescence of these smaller droplets. A comparative analysis of dead-end chambers with varying neck dimensions reveals that larger condensed droplet volumes correlate with an increased number of compartments, as shown in Fig. S5a. However, without the assistance of gravity, the separate coacervate droplets will not condense into a single coacervate, as shown in Fig. S5b. During the fusion process, in the large fused droplets, we observe the formation of internal compartments, which are not observed within the smaller coacervates.

Interestingly, we also observe the reversible formation of such internal compartments upon subtle changes in the external chemical composition; these compartments can be formed in a repeatable way by controlling the composition of the flow in the main channel of our devices. To investigate this reversible compartmentalization and to reduce the loss of polymers during long-term experiments, we next choose experimental conditions where the polymer concentration in the continuous phase is lower. We thus employ a 1.0 M KCl

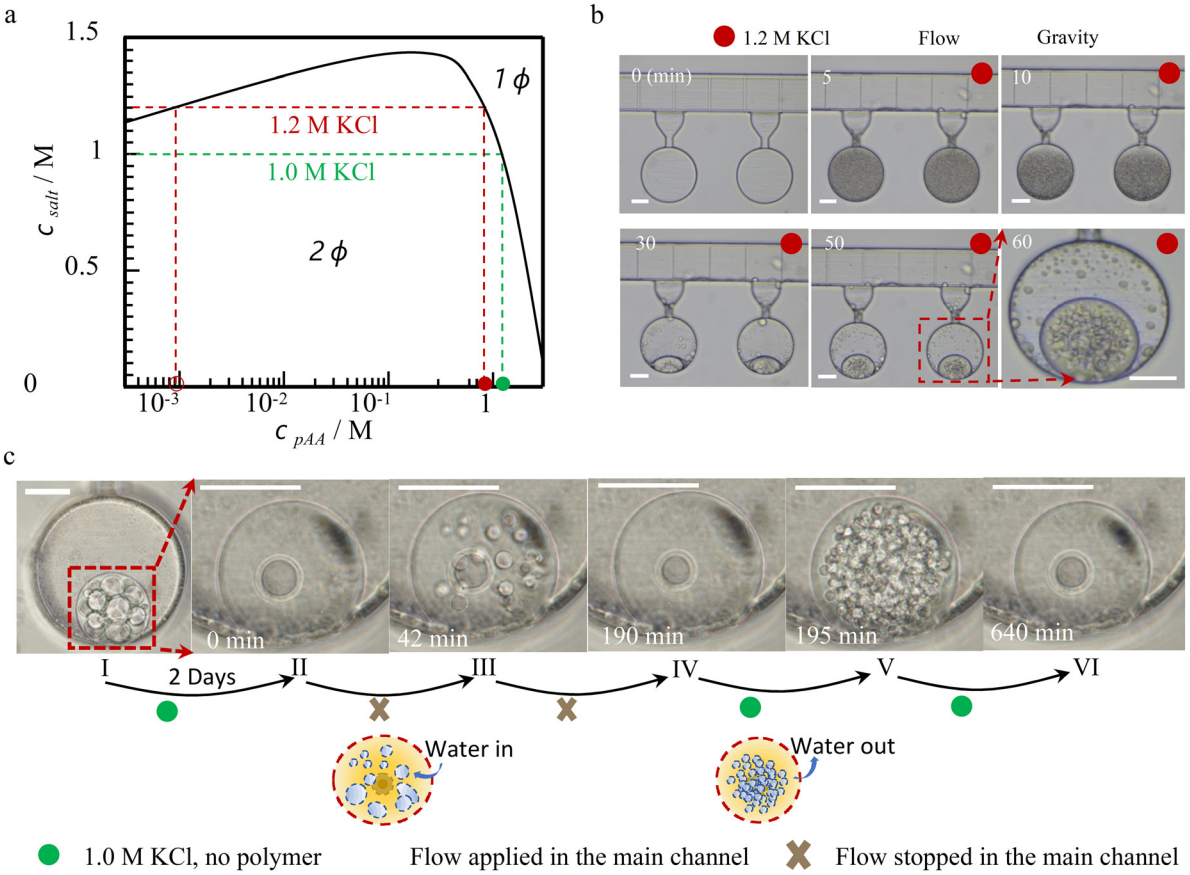

Fig. 4 Associative formation and reversible compartmentalization of water-in-water (W/W) droplets *via* coacervate phase separation. a, Phase diagram showing the associative complex coacervate formation within the PAA–PDMAEMA system (100 kDa for PAA and 104 kDa for PDMAEMA) when choosing pH = 6.5 (±0.2) to regulate 1 : 1 positive–negative charge density ratio. b, The coacervate generation process in dead-end chambers: step 1, the device is filled with a homogeneous solution of 0.33 M PAA and 0.33 M PDMAEMA diluted in 1.5 M KCl; step 2, starting at 5 min, a 1.2 M KCl solution is injected to induce phase separation and the device is tilted to a vertical position facilitating the coalescence of separated coacervates at the bottom of the dead-end chamber. Multiple compartments are observable within a single coacervate droplet at 60 minutes. c, Sequential images illustrating the reversible compartmentalization process: image I, initial formation of coacervates with multiple compartments under 1.0 M KCl flow in the main channel; image II, state after a 2 day equilibration period, during which all but one of the compartments disappear; image III, compartments reform after stopping the flow of 1.0 M KCl in the main channel; image IV, after 148 minutes of re-equilibration, the coacervate droplet reverts to its previous state; image V, upon the resumption of the 1.0 M KCl flow, compartments within the coacervates are formed again rapidly within 5 minutes. Image VI, eventually, the coacervate droplet reaches the next quasi-equilibrium state with multiple compartments gradually disappearing. Time scales at the bottom left of images II–VI indicate the time after cessation of 1.0 M KCl flow. The schematic diagrams correspond to the transitions from image II–III and IV–V, illustrating the flux of water into and out of the coacervate, respectively. Scale bars are 100 μm for all images.

solution to generate coacervate droplets. Initially, in analogy to the previous experiments performed at 1.2 M KCl, we obtain a single coacervate droplet containing numerous compartments, as shown in image I in Fig. 4c. After maintaining a constant flow of the 1.0 M KCl solution (at a flow rate of 100 μl h^{-1}) in the main channel for two days, we observe that the compartments within the coacervate droplet gradually disappear, as shown in image II in Fig. 4c and S5c, where only one single compartment remains within the coacervate. Subsequently, when we stop the flow in the main channel, we notice that the droplet absorbs water and swells slightly, producing multiple compartments within the coacervate at the 42 minute mark (image III in Fig. 4c). After another 148 minutes, the microenvironment within the dead-end chamber reaches the next quasi-equilibrium state, at which the compartments have dissolved and vanished, with only one compartment remaining (image IV in Fig. 4c). However, when we resume the 1.0 M KCl flow in the main channel, the compartmentalization process within the coacervate droplet restarts, generating multiple compartments in a short period (image V in Fig. 4c). These compartments again gradually disappear as the microenvironment within the dead-end chamber equilibrates (image VI in Fig. 4c).

We thus find a straightforward way to regulate the reversible compartmentalization process inside a membraneless coacervate droplet containing only two polymer components. This is in contrast to previous reports on compartmentalization within coacervates, which are generally executed in bulk solution with three or more components or where solvent and/or temperature conditions are drastically changed.[24–26]

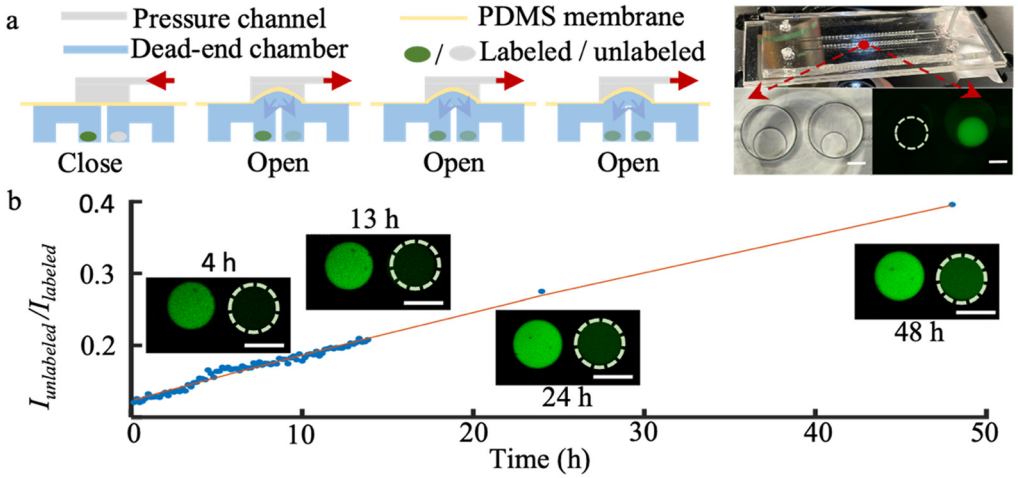

Fig. 5 Inter-droplet communication within a microfluidic chip. a, Left: schematic illustration of the valve mechanism enabling controlled inter-droplet communication. The microfluidic device comprises three primary elements: a pneumatic pressure control channel, a PDMS membrane, and two independent dead-end chambers (similar to the ones shown in Fig. 2a). Right: photo of the device and microscopic images (bright field and fluorescent) of two dextran droplets (one fluorescently labeled with FITC, and the other unlabeled) in communicating channels connected by a pneumatic valve. b, Plot of the intensity ratio ($I_{unlabeled}/I_{labeled}$) as time proceeds, and a linear fit to the data. Scale bars: 100 μm.

We also test the possibility of creating such coacervates with internal compartments using devices made of polydimethylsiloxane (PDMS) by standard soft lithography, as shown in Fig. S7f. However, although we observe phase separation into a large number of small droplets, these droplets do not merge into one large coacervate, even when gravity is applied. It seems that the droplets stick to the surface of the PDMS, or that the coacervate phase even spreads across the surface of the PDMS device. This further illustrates the advantages of using our glass microfluidic devices fabricated by femtosecond laser machining.

Extension to study inter-chamber communication

Our method allows us to fine-tune conditions in many fluidic chambers, as controlled by diffusion between them and a main channel. However, the basic method does not enable us to study the interaction between droplets with different compositions and structures, which could be interesting, for instance, for studying spatiotemporal communication between macromolecular condensates in biological cells and in synthetic analogs that mimic their behavior.

Spatiotemporal control of communication between intracellular compartments and synthetic analogs is of great interest. While the controlled communication between membrane-protected compartments and non-fusing membraneless droplets has been studied previously using traditional methods, a precise control and study of the spatiotemporal communication between membraneless and fusing droplets remains challenging.[27] Therefore, we aim to extend our method to enable the controlled and triggered interaction between two microfluidic chambers. In doing so, we demonstrate that distance-controlled communication between two different membraneless droplets can be precisely regulated and programmed with our microfluidic system. As shown in Fig. 5a, we introduce a pressure channel equipped with an array of pneumatic micro-valves (grey) and a 150 μm-thick PDMS membrane (yellow) to control connections between two independent dead-end chambers (blue) in which labeled and unlabeled dextran droplets are formed independently (Fig. 5a and S6a–c SI). A positive pressure on the pneumatic valves results in the PDMS membrane closing the connection between the two chambers, allowing for independent preparations of different types of droplets *in situ*. When negative pressure is applied, the PDMS membrane is lifted, opening the pneumatic valve and establishing a connection between the two chambers.

To test this system, we perform communication experiments between two separate chambers containing droplets formed from dextran-FITC fluorescently labeled dextran and unlabeled dextran, respectively. As shown in Fig. 5b, we observe a gradual diffusion of dextran-FITC from one droplet to the other when the connection between two chambers is opened. The communication rate can be adjusted by changing the size of the dead-end chambers or by employing polymers of different chain lengths.

This demonstrates the potential to realize communication between chambers in a controllable fashion in our devices. Following designs could enable the adaptation of our method to the spatiotemporal control of communicating systems, for instance in the study of complex cell–cell interactions, allowing a detailed analysis of chemical signal transmission between biological cells.

Conclusion

This work introduces a microfluidic method that provides precise control over liquid–liquid phase separation (LLPS) in water-in-water (W/W) systems, effectively addressing the challenges posed by the low surface tension inherent to these systems. Our method enables droplet generation, confinement

and stabilization within microfluidic dead-end chambers without additional encapsulants or surface modifications, which are generally necessary when using traditional approaches.[14,28–30] This development offers a robust and versatile tool for studying and controlling the complex dynamics of LLPS in a precisely controlled environment.

We validated our method using the PEG/dextran system, achieving exceptional control over droplet size and solute concentrations. This level of precision surpasses that of conventional techniques, which often struggle with variability and instability in W/W systems. The consistent production of uniform droplet populations marks a significant advancement, particularly for applications in synthetic biology, drug delivery, and diagnostics, where uniformity is crucial.

Another advantage of our method is the ability to study individual droplets over long periods of time while keeping the conditions fixed. This is enabled by the inherent compartmentalization and immobilization of the droplets within the microfluidic chambers of the device. Moreover, by using devices made from glass, we circumvent the evaporation of solvents and diffusion of compounds into the bulk of the microfluidic device, which is a common problem in conventional microfluidic devices made from the elastomer polydimethylsiloxane (PDMS). In our glass devices, conditions can be kept stable for days without changes in concentrations caused by evaporation or diffusion.

To illustrate the versatility of our method, we investigated its applicability to the study of associative LLPS using the PAA/PDMAEMA system. We demonstrated the ability to induce and reversibly control compartmentalization within coacervate droplets, which typically necessitates drastic changes in environmental conditions and often results in irreversible system alterations. Our method's capacity to fine-tune the internal structure of coacervates through simple flow adjustments enables the exploration of cellular processes and the origins of life with a level of detail that was previously challenging to achieve.

Despite these advantages, the present implementation has several practical limitations. Inter-droplet exchange is primarily diffusion-controlled, so the characteristic response times depend on molecular diffusivity and device geometry, with variations in viscosity or interfacial tension mainly affecting the kinetics rather than the feasibility of the approach. In addition, achieving independent and dynamic control over the composition of multi-component inner phases remains challenging in the current configuration. Finally, stable droplet formation relies on appropriate wettability and density matching between phases, which limits the compatibility of certain ATPS combinations. These limitations may be addressed through targeted optimization of device design and surface properties. In particular, modifying chamber geometry and connecting neck dimensions—such as widening or shortening the necks or reducing the size of the dead-end chambers—is a straightforward way to enhance molecular exchange. In addition, tailoring surface wettability and chamber architecture may broaden compatibility with more complex ATPS compositions and improve control over multi-component systems.

Moreover, the integration of pneumatically controlled valves into our method facilitates controlled communication between distinct droplets, a critical feature for the advancement of synthetic cells and complex biochemical networks. This valve-based control enables communication to be initiated, modulated in intensity, or completely halted on demand, providing dynamic regulation of inter-droplet exchange. Precise spatiotemporal control of inter-droplet interactions, as demonstrated in our study, opens the door to more complex investigations of multi-compartmentalized systems, with significant implications for synthetic biology and materials science.

Author contributions

Conceptualization: CL, HF, HMW. Methodology: CL, HF. Investigation: CL, HF, KJB. Visualization: CL, HMW. Supervision: HMW, SH. Writing – original draft: CL, HF, HMW. Writing – review & editing: CL, HF, KJB, JMJT, SH, HMW.

Conflicts of interest

There are no conflicts to declare.

Data availability

All data are available in the main text or the supplementary information (SI).

Supplementary information: the SI contains a PDF with supplementary figures, detailed experimental methods, additional supporting data, and captions for supplementary movies. See DOI: https://doi.org/10.1039/d5lc01055a.

Acknowledgements

We thank W. Liu and Z. W. Cui for helpful discussions, M. K. Seveda and T. ul-Islam for technical guidance. CL thanks the China Scholarship Council for financial support. KJB and HMW are grateful for support from the IDEAS institute, a collaboration between Zhejiang University, Hangzhou, China, and Eindhoven University of Technology (TU/e), financially supported by the board of TU/e. HF and EWM are supported by the Royal Netherlands Academy of Science.

References

1 Y. Sun, N. Yu, J. Zhang and B. Yang, *Micromachines*, 2025, **16**, 426.
2 W.-M. Zhou, Y.-Y. Yan, Q.-R. Guo, H. Ji, H. Wang, T.-T. Xu, B. Makabel, C. Pilarsky, G. He, X.-Y. Yu and J.-Y. Zhang, *J. Nanobiotechnol.*, 2021, **19**, 312.
3 S. Yoon, D. Kilicarslan You, U. Jeong, M. Lee, E. Kim, T.-J. Jeon and S. M. Kim, *Biosensors*, 2024, **14**, 55.
4 W. E. Arter, R. Qi, N. A. Erkamp, G. Krainer, K. Didi, T. J. Welsh, J. Acker, J. Nixon-Abell, S. Qamar, J. Guillén-Boixet, T. M. Franzmann, D. Kuster, A. A. Hyman, A. Borodavka,

P. S. George-Hyslop, S. Alberti and T. P. J. Knowles, *Nat. Commun.*, 2022, **13**, 7845.
5 D. Saeki, S. Sugiura, T. Kanamori, S. Sato and S. Ichikawa, *Lab Chip*, 2010, **10**, 357–362.
6 T. Beneyton, C. Love, M. Girault, T.-Y. D. Tang and J. Baret, *Chem*, 2020, **2**, e2000022.
7 D. Onan, M. Özder, M. İ. Sipahi, N. Poyraz, C. Apaydın, G. Erel-Akbaba and H. Akbaba, *J. Biomed. Mater. Res., Part B*, 2025, **113**, e35530.
8 Y. Chao and H. C. Shum, *Chem. Soc. Rev.*, 2020, **49**, 114–142.
9 C. Xu, N. Martin, M. Li and S. Mann, *Nature*, 2022, **609**, 1029–1037.
10 Y. Minagawa, M. Yabuta, M. Su'etsugu and H. Noji, *Nat. Commun.*, 2025, **16**, 1522.
11 F. Peters and D. Arabali, *Colloids Surf., A*, 2013, **426**, 1–5.
12 E. Atefi, J. A. Mann and H. Tavana, *Langmuir*, 2014, **30**, 9691–9699.
13 M. G. F. Last, S. Deshpande and C. Dekker, *ACS Nano*, 2020, **14**, 4487–4498.
14 S. Deshpande, F. Brandenburg, A. Lau, M. G. F. Last, W. K. Spoelstra, L. Reese, S. Wunnava, M. Dogterom and C. Dekker, *Nat. Commun.*, 2019, **10**, 1800.
15 B.-U. Moon, N. Abbasi, S. G. Jones, D. K. Hwang and S. S. H. Tsai, *Anal. Chem.*, 2016, **88**, 3982–3989.
16 H. Zhu, P. Zhang, Z. Zhong, J. Xia, J. Rich, J. Mai, X. Su, Z. Tian, H. Bachman, J. Rufo, Y. Gu, P. Kang, K. Chakrabarty, T. P. Witelski and T. J. Huang, *Sci. Adv.*, 2021, **7**, eabc7885.
17 X. Guan, G. Cheng, Y.-P. Ho, B. P. Binks and T. Ngai, *Small*, 2023, **19**, e2304207.
18 S. LoTurco, R. Osellame, R. Ramponi and K. C. Vishnubhatla, *J. Micromech. Microeng.*, 2013, **23**, 85002.
19 Y. Wang, S. Chen, H. Sun, W. Li, C. Hu and K. Ren, *Microphysiol. Syst.*, 2018, **2**(6), DOI: 10.21037/mps.2018.08.02.
20 A. D. Diamond and J. T. Hsu, *Biotechnol. Tech.*, 1989, **3**, 119–124.
21 C. D. Crowe and C. D. Keating, *Langmuir*, 2022, **38**, 1811–1820.
22 M. Naz, L. Zhang, C. Chen, S. Yang, H. Dou, S. Mann and J. Li, *Commun. Chem.*, 2024, **7**, 79.
23 J. van der Gucht, E. Spruijt, M. Lemmers and M. A. Cohen Stuart, *J. Colloid Interface Sci.*, 2011, **361**, 407–422.
24 T. Lu and E. Spruijt, *J. Am. Chem. Soc.*, 2020, **142**, 2905–2914.
25 N. A. Erkamp, T. Sneideris, H. Ausserwöger, D. Qian, S. Qamar, J. Nixon-Abell, P. St George-Hyslop, J. D. Schmit, D. A. Weitz and T. P. J. Knowles, *Nat. Commun.*, 2023, **14**, 684.
26 N. A. Erkamp, M. A. M. Verwiel, D. Qian, T. Sneideris, F. A. Spaepen, D. A. Weitz, J. C. M. Van Hest and T. P. J. Knowles, *Nat. Chem. Eng.*, 2024, **1**, 430–439.
27 A. Joesaar, S. Yang, B. Bögels, A. van der Linden, P. Pieters, B. V. V. S. P. Kumar, N. Dalchau, A. Phillips, S. Mann and T. F. A. de Greef, *Nat. Nanotechnol.*, 2019, **14**, 369–378.
28 N.-N. Deng and W. T. S. Huck, *Angew. Chem., Int. Ed.*, 2017, **56**, 9736–9740.
29 K. D. Seo, S. Shin, H. Y. Yoo, J. Cao, S. Lee, J.-W. Yoo, D. S. Kim and D. S. Hwang, *Biomacromolecules*, 2020, **21**, 930–938.
30 I. Ziemecka, V. van Steijn, G. J. M. Koper, M. T. Kreutzer and J. H. van Esch, *Soft Matter*, 2011, **7**, 9878–9880.